Chemical Science

ROYAL SOCIETY OF CHEMISTRY

EDGE ARTICLE

View Article Online
View Journal | View Issue

Cite this: *Chem. Sci.*, 2022, **13**, 497

All publication charges for this article have been paid for by the Royal Society of Chemistry

Unleashing non-conjugated polymers as charge relay mediators†

Bi-Jian Liu,[a] Hao Liang,[a] Qiao-Ling Mo,[a] Shen Li,[a] Bo Tang,[a] Shi-Cheng Zhu[a] and Fang-Xing Xiao *[ab]

The core factors affecting the efficiency of photocatalysis are predominantly centered on controllable modulation of anisotropic spatial charge separation/transfer and regulating vectorial charge transport pathways in photoredox catalysis, yet it still meets with limited success. Herein, we first conceptually demonstrate the rational design of unidirectional cascade charge transfer channels over transition metal chalcogenide nanosheets (TMC NSs: $ZnIn_2S_4$, CdS, $CdIn_2S_4$, and In_2S_3), which is synergistically enabled by a solid-state non-conjugated polymer, *i.e.*, poly(diallyldimethyl ammonium chloride) (PDDA), and MXene quantum dots (MQDs). In such elaborately designed photosystems, an ultrathin PDDA layer functions as an intermediate charge transport mediator to relay the directional electron transfer from TMC NSs to MQDs that serve as the ultimate electron traps, resulting in a considerably boosted charge separation/migration efficiency. The suitable energy level alignment between TMC NSs and MQDs, concurrent electron-withdrawing capabilities of the ultrathin PDDA interim layer and MQDs, and the charge transport cascade endow the self-assembled TMC/PDDA/MQD heterostructured photosystems with conspicuously improved photoactivities toward anaerobic selective reduction of nitroaromatics to amino derivatives and photocatalytic hydrogen evolution under visible light irradiation. Furthermore, we ascertain that this concept of constructing a charge transfer cascade in such TMC-insulating polymer-MQD photosystems is universal. Our work would afford novel insights into smart design of spatial vectorial charge transport pathways by precise interface modulation *via* non-conjugated polymers for solar energy conversion.

Received 3rd September 2021
Accepted 5th December 2021

DOI: 10.1039/d1sc04877e

rsc.li/chemical-science

1. Introduction

The critical challenges facing the world nowadays are predominantly centered on energy deficiency and environmental pollution, urgently calling for new technologies to alleviate these problems for sustainable development of human beings in the near future. Semiconductor-based heterogeneous photocatalysis represents a promising and green technology to enable clean energy production and environmental remediation *via* solar energy conversion.[1,2] Among the diverse nanostructured semiconductors, two-dimensional (2D) layered transition metal chalcogenides (TMCs), in which six chalcogen atoms and transition metals bond with each other to form the layered structure under the pull of covalent bonds, have garnered enduring interest owing to the advantageous physicochemical properties and unique structural merits such as substantial light-harvesting capability, abundant active sites, short mean free paths of charge transfer and favorable energy level alignment,[3–5] making TMC-based heterostructures applicable photocatalysts for multifarious photoredox catalysis such as photocatalytic hydrogen generation, CO_2 photoreduction, and photocatalytic selective organic transformation.[6–10] Nevertheless, the high electron–hole recombination rate, slow carrier migration kinetics and intrinsic instability of TMCs hinder their wide-spread photocatalytic applications.[11] To surmount these obstacles, diverse strategies have thus been presented such as metal or non-metal element doping, interface engineering, and heterojunction modulation.[12–15] Despite the advancements, fabricating robust and stable TMC-based heterostructured photosystems still remains challenging.

More recently, MXenes, as novel 2D transition metal carbides, carbonitrides or nitrides, stand out among diverse 2D materials as promising co-catalysts for constructing a built-in electric field to accelerate charge separation/transfer owing to their excellent electrical conductivity, favorable Fermi level position and abundant active sites.[16–18] It is noteworthy that MXene quantum dots (MQDs), which inherit the generic advantages of MXenes, feature superior quantum confinement effect, fascinating photoluminescence performance and more abundant active sites.[19,20] Moreover, the good hydrophilicity of

[a]*College of Materials Science and Engineering, Fuzhou University, New Campus, Minhou, Fujian Province, 350108, China. E-mail: fxxiao@fzu.edu.cn*

[b]*Fujian Science & Technology Innovation Laboratory for Optoelectronic Information of China, Fuzhou, Fujian 350108, P. R. China*

† Electronic supplementary information (ESI) available. See DOI: 10.1039/d1sc04877e

MQDs makes them an alternative building block to construct elegant self-assembled composite photosystems with other semiconductors.[21] Nevertheless, so far, studies on MQDs as a charge transfer mediator in solar-powered photocatalysis especially in selective organic transformation and hydrogen generation have seldom been reported.

Polyelectrolytes (PEs), which are defined as polymers with positively or negatively charged properties in repeating monomeric units,[22,23] have been extensively utilized as surface charge modifiers to fabricate spatially multilayered multi-dimensional nano-architectures in a precise, controllable and exquisite manner at the nanoscale level.[24–27]In these ways, PEs mainly play a crucial role as self-assembly initiators, by which oppositely charged building blocks are well organized into well-defined heterostructures. However, utilizing PEs that are mainly composed of non-conjugated polymers as the carrier mediator to regulate the vectorial charge transport pathways has so far not yet been reported in terms of their intrinsic insulating properties in the solid state.[28–30]Considering the integrated superiorities of PEs and possible charge transport capability, we deduce that PE-involved self-assembly would significantly favor construction of heterostructured photosystems *via* suitable interface engineering, and more importantly, would concurrently afford regulated vectorial charge transfer modulation.

Herein, inspired by these motivations, oppositely charged poly(diallyldimethyl ammonium chloride) (PDDA) and MQDs are harnessed as the building blocks for crafting spatially multilayered TMC/PDDA/MQD heterostructures, wherein a solid-state ultra-thin PDDA intermediate layer and MQDs are progressively self-assembled on TMC NSs *via* electrostatic interactions. We found that the synergy of the ultrathin PDDA interim layer and ultra-small MQDs stemming from their concurrent electron-withdrawing capabilities contributes to the cascade charge transfer channel. This unique charge transport pathway endows the TMC/PDDA/MQD heterostructures with markedly enhanced and versatile photoactivities toward anaerobic selective reduction of aromatic nitro compounds to amino derivatives and photocatalytic hydrogen evolution under visible light irradiation. This is predominantly ascribed to the crucial role of the ultrathin PDDA interim layer that acts as an efficient interfacial electron transport mediator to relay the electrons photoexcited from TMC NSs, while MQDs function as the terminal electron acceptors to accelerate the unidirectional charge transport from TMC NSs to MQDs, resulting in markedly enhanced charge separation. Furthermore, we also ascertain that the concept of crafting such a unidirectional cascade charge transfer channel is universal. Our work would unleash the long-term ignored charge transfer capability of non-conjugated polymers for solar energy conversion.

2. Experimental section

2.1 Preparation of TMC nanosheets (NSs)

TMC NSs including $ZnIn_2S_4$ (ZIS), CdS, $CdIn_2S_4$ (CIS) and In_2S_3 (IS) were fabricated by a low-temperature refluxing method,[31,32] and CdS NSs were prepared *via* a hydrothermal method.[17] Detailed information on the synthetic procedures is provided in the ESI.†

2.2 Preparation of Ti_3C_2 QDs (MXene QDs)

Preparation of MXene QDs (MQDs) is carried out according to a previously published study.[18] Detailed synthetic procedures are provided in the ESI.†

2.3 Preparation of TMC/PDDA binary nanocomposites

ZIS NSs were selected as the representative TMC NSs for systematic investigation. Specifically, ZIS (100 mg) was added into 10 mL of PDDA aqueous solution (0.5 M NaCl, pH = 10) with a concentration of x (x = 5, 10, 15, and 20 mg mL^{-1}), and vigorously stirred for 1 h. After that, the mixture was centrifuged, and the thus-obtained PDDA-modified ZIS (ZP-x) nanocomposites were thoroughly washed with deionized (DI) H_2O to remove residual free PDDA adsorbed on the surface. Finally, the obtained powder was dried in a vacuum at 333 K for 12 h. Preparation of CdS/PDDA, CIS/PDDA and IS/PDDA nanocomposites is analogous to that of ZP-10 except that the ZIS NS substrate was replaced with CdS, CIS or IS NSs, respectively.

2.4 Preparation of TMC/PDDA/MQD ternary nanocomposites

ZIS/PDDA/MQD (ZPM) nanocomposites were fabricated *via* an electrostatic self-assembly method under ambient conditions. In detail, the ZP-10 nanocomposite (100 mg) was added into x (x = 5, 10, 15, 20) mL of MQD aqueous solution (25 ppm, pH = 9) and stirred for 1 h, and then the mixture was collected by centrifugation and dried in a vacuum at 333 K for 12 h to obtain ZPM-x. Preparation of CdS/PDDA/MQD, CIS/PDDA/MQD and IS/PDDA/MQD nanocomposites is analogous to that for ZPM-10 except that ZP-10 was replaced with CdS/PDDA, CIS/PDDA or IS/PDDA, respectively.

2.5 Characterization

The crystal structure of the catalysts was determined by X-ray diffraction (XRD) (Miniflex600). UV-vis diffuse reflectance spectra (DRS, Cary50, Varian, America) were measured on a Varian Cary 500 using $BaSO_4$ as the reference background. Fourier transform infrared (FTIR) spectroscopy was performed on a TJ270-30A infrared spectrophotometer (Tianjin, China). The Brunauer–Emmett–Teller (BET) specific surface area was detected using a Quantachrome Autosorb-1-C-TCD automated gas sorption analyzer. Raman spectra were recorded on a Thermo Scientific Dxr-2xi Raman imaging microscope. Morphologies of the samples were collected by using a Carl Zeiss Supra55 field-emission scanning electron microscope (FESEM). TEM images of the samples were recorded with a Tecnai G2 F20 transmission electron microscope (200 kV). X-ray photoelectron spectroscopy (XPS) was performed on an ESCALAB 250 (Thermo Scientific, America), and 284.6 eV of the C 1s peak was used to correct the binding energy (B.E.). Photoluminescence (PL) spectra of the catalyst were recorded by using a Varian Cary Eclipse spectrometer. Zeta potentials were

recorded by dynamic light scattering analysis (Zetasizer Nano ZS-90).

2.6 Photocatalytic selective organic transformation

Photocatalytic reduction of nitroaromatics to amino compounds was probed under the irradiation of a 300 W Xe lamp (PLS-SXE300D, Beijing Perfect Light Co. Ltd, China) equipped with a 420 nm cut-off filter under ambient conditions. The detailed procedures are as follows:10 mg of catalyst and 40 mg of sodium sulfite (Na_2SO_3) as the hole scavenger were mixed with 30 mL of 4-NA (5 ppm) under N_2 bubbling. Subsequently, the mixed solution was stirred in the dark for 15 min to achieve the adsorption–desorption equilibrium between the reactant and catalyst before irradiation. 3 mL of the sample solution was taken out at a given time (0, 5, 10, 15, 20, and 25 min) and centrifuged to obtain the supernatant. Then, the supernatant was analyzed by using an UV-vis absorption spectrophotometer (Thermal Fisher, GENESYS). The photoactivity of the sample is defined by the following formula:

$$\text{Conversion}\% = \frac{C_0 - C}{C_0} \times 100\%$$

where C_0 represents the initial concentration of nitroaromatics, and C is the concentration after visible light irradiation for a certain time.

2.7 Photocatalytic hydrogen evolution

The catalyst (10 mg) was dispersed in 5 mL of DI H_2O containing 0.625 M Na_2SO_3 and 0.75 M Na_2S, which were used as the sacrificial reagents. The visible light source was provided by a 300 W Xe lamp (PLS-SXE300D, Beijing Perfect Light Co. Ltd, China) equipped with a 420 nm cut-off filter. Hydrogen evolution was analyzed on a gas chromatograph (Shimadzu GC-8A) utilizing argon as the carrier gas. The apparent quantum yield (A.Q.Y) and solar-to-hydrogen (S.T.H) conversion efficiency were investigated according to the previous studies based on the following definition:[33–35]

$$\text{A.Q.Y}(\%) = \frac{\text{number of reacted electrons}}{\text{number of incident photon}} \times 100\%$$

$$= \frac{\text{number of evolved hydrogen molecules} \times 2}{\text{number of incident photon}} \times 100\%$$

$$\text{S.T.H} = \frac{n_{H_2}(\text{mmol}) \times \Delta G(\text{KJ mol}^{-1})}{S(\text{cm}^2) \times P(\text{mW cm}^{-2}) \times t(\text{s})} \times 100\%$$

where n_{H_2} is the amount of H_2 molecules, ΔG is the Gibbs free energy per mol of H_2 (at 25°C and $\Delta G = 237$ kJ mol^{-1}), S is the irradiation area, P is the light intensity, and t is the reaction time.

2.8 Photoelectrochemical (PEC) performances

PEC measurements were carried out on an electrochemical workstation (CHI 660E and Gamary Interface 1000 E) with a conventional three-electrode quartz cell using 0.5 M Na_2SO_4 aqueous solution (100 mL, 0.5 M, and pH = 6.69) as the electrolyte and Pt & Ag/AgCl electrodes as the counter and reference electrodes, respectively. Potentials are calibrated according to the formula given below:

$$E_{RHE} = E_{Ag/AgCl} + 0.0591\text{pH} + 0.1976$$

Detailed information on the fabrication of working electrodes is provided in the ESI.†

3. Results and discussion

3.1 Structural characterization

The schematic synthesis procedure of TMC/PDDA/MQD nanocomposites is illustrated in Fig. 1a, wherein tailor-made positively charged PDDA-modified TMC NSs and negatively charged MQDs are chosen as the building blocks. Herein, the ZIS NS substrate is selected as the representative TMC NSs to elucidate the electrostatic self-assembly buildup. TEM images (Fig. S1a & b†) and the size distribution histogram (Fig. S1c†) of MQDs reveal their mean size of *ca.* 2.4 nm. Meanwhile, PL spectra (Fig. S1d†) verify the successful fabrication of the MQD colloidal aqueous solution. Surface charge properties of ZIS NSs, ZP and MQDs were determined by the zeta potential measurements. As shown in Fig. S2,† ZIS NSs feature a negatively charged surface within a wide pH range (2–12), and ZP shows a positively charged surface with a zeta potential of +37.9 mV due to the quaternary ammonium functionality from PDDA, which implies that PDDA encapsulation helps to transform the surface charge properties of ZIS from intrinsically negatively charged (Fig. S2†) to positively charged (Fig. S3†). In contrast, MQDs demonstrate a negatively charged surface (Fig. S4†), which lays a solid foundation for electrostatic self-assembly with the oppositely charged ZP. Therefore, electrostatic interactions between ZP and MQDs allow the spontaneous self-assembly of ZPM nanocomposites under ambient conditions. The UV-vis absorption spectrum of MQDs provides an effective tool to monitor the electrostatic self-assembly process. Specifically, with regard to the UV-vis absorption spectrum of the supernatant of the MQD colloidal aqueous solution, a decreased peak intensity of MQDs was observed after being vigorously stirred with ZP compared with that of the original MQDs (Fig. S5†), implying deposition of MQDs on the ZP surface.

XRD was utilized to probe the crystallographic structures of the samples. As shown in Fig. 1b, XRD patterns of ZIS, ZP and ZPM are similar, for all of which the characteristic peaks at 21.6°, 27.7°, 30.4°, 39.8°, 47.2° and 52.4° are attributed to the (006), (102), (104), (108), (110) and (116) crystal facets of the hexagonal $ZnIn_2S_4$ phase (JCPDS no.65-2023).[32] However, XRD patterns of ZP and ZPM are analogous to that of ZIS, revealing that the crystal structure of ZIS is retained after PDDA encapsulation and electrostatic MQD deposition. Moreover, no obvious peak attributable to MQDs can be distinguished in the XRD pattern of ZPM, which might be ascribed to the relatively weak peak intensity of MQDs or the peaks are shielded by the main diffraction peaks of the ZIS substrate.

Optical properties of the samples were measured from UV-vis diffuse reflectance spectra (DRS). As displayed in Fig. 1c, the

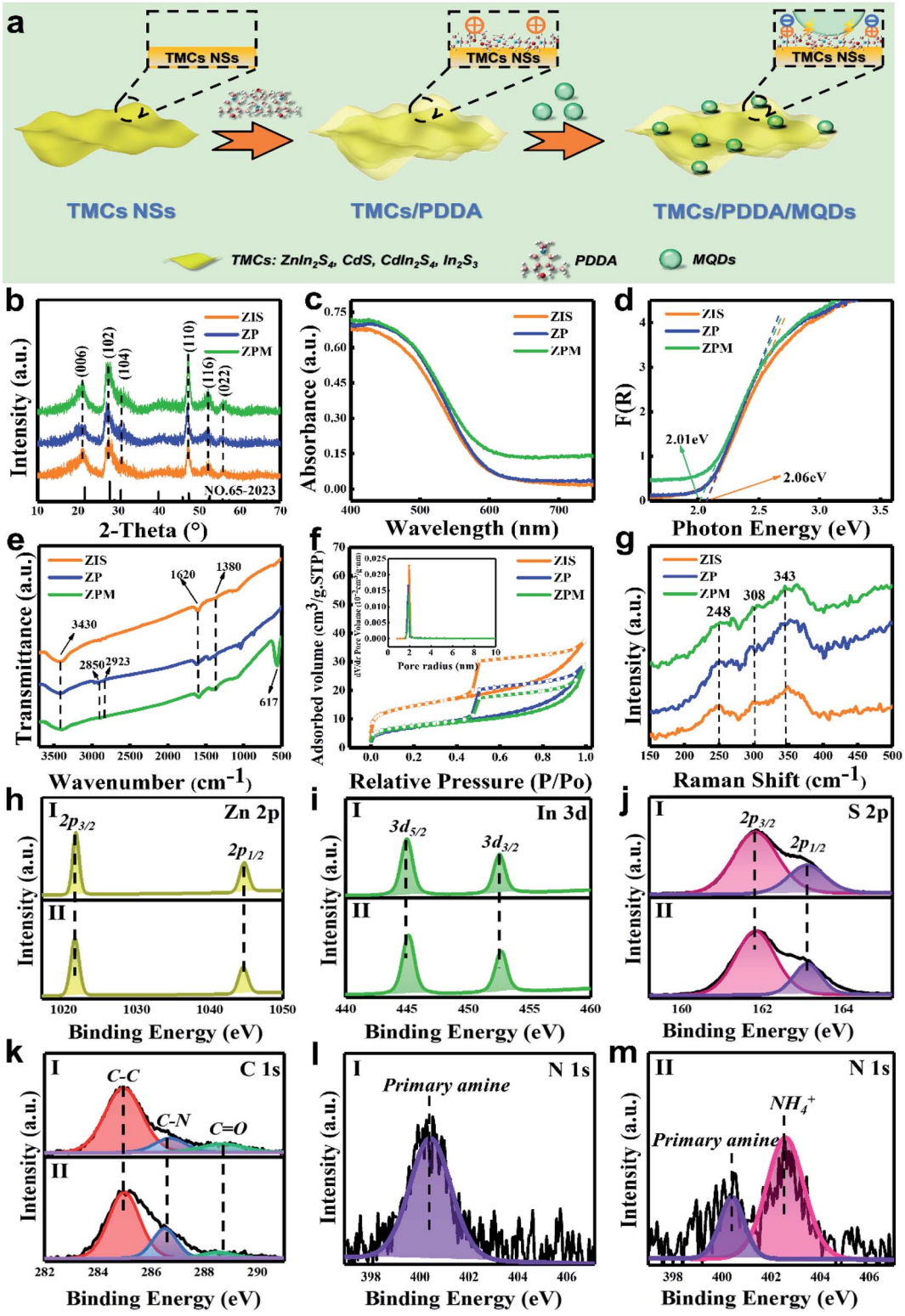

Fig. 1 (a) Schematic flowchart of the fabrication of TMC/PDDA/MQD nanocomposites. (b) XRD patterns and (c) DRS results with (d) transformed plots based on the Kubelka–Munk function *vs.* photon energy for ZIS, ZP and ZPM; (e) FTIR spectra of ZIS, ZP and ZPM, and (f) N_2 adsorption–desorption isotherms of ZIS, ZP and ZPM with pore size distribution in the inset. (g) Raman spectra of ZIS, ZP and ZPM. High-resolution (h) Zn 2p, (i) In 3d, (j) S 2p, and (k) C 1s, and (l & m) N 1s spectra of (I) ZIS and (II) ZPM.

light absorption band edge of all these samples approaches 610 nm, which is attributed to the band-gap photoexcitation of the ZIS substrate.[31] It is worth noting that PDDA encapsulation exerts no substantial effect on the light absorption of ZIS NSs. This is consistent with the UV-vis absorption spectrum of the PDDA aqueous solution (Fig. S6†) which does not show

absorption in the visible region, indicating that PDDA does not affect the optical properties of the ZP nanocomposite. Moreover, the absorption band edge of ZPM is similar to that of ZIS and ZP, which we believe is mainly due to the intrinsic absence of light absorption of MQDs in the visible domain, as evidenced by the UV-vis absorption of the MQD aqueous solution (Fig. S5†).[36] In other words, MQD deposition fails to affect the light absorption of ZPM but rather serves as a charge mediator which will be elucidated in the latter part. Similar light absorption of ZIS, ZP and ZPM can also be reflected by their unchanged colors (Fig. S7†). Besides, based on the transformed Kubelka–Munk function *vs.* the energy of light, bandgaps (E_g) of ZIS, ZP and ZPM are determined to be 2.06eV, 2.06eV and 2.01eV (Fig. 1d), respectively. The results imply that E_g values of ZP and ZPM are not affected by PDDA encapsulation and MQD deposition.

As displayed in Fig. 1e and Table S1,† the FTIR result of ZIS exhibits three typical peaks at 3430, 1620 and 1380 cm^{-1} which correspond to the –NH, –CONH– and deformative vibration mode of $–CH_3$ from the ZIS precursor (TAA).[31,37] FTIR spectra of ZP and ZPM exhibit two peaks at 2923 and 2850 cm^{-1} corresponding to the bending vibration mode of the methylene ($–CH_2$) group,[25,28] which originate from the ultra-thin PDDA layer, indicating that PDDA has been encapsulated on the ZIS NS surface. Notably, an exclusive peak at 617cm^{-1} is visualized in the FTIR spectrum of ZPM, which is attributed to the Ti–C species from MQDs,[16,20] indicating that MQDs have been successfully grafted on the ZP nanocomposite *via* electrostatic forces. As shown in Fig. 1f, ZIS, ZP and ZPM display the type-IV isotherms according to the IUPAC classification in N_2 adsorption–desorption measurements, implying that all the samples belong to the typical mesoporous material. As summarized in Table S2,† specific surface areas of ZIS, ZP and ZPM are determined to be 51.74, 23.00 and 24.83 $m^2\ g^{-1}$, respectively. Compared with ZIS, the specific surface area of ZP is reduced to some extent, which may be caused by the agglomeration of ZIS NSs after PDDA encapsulation. ZPM demonstrates almost the same specific surface area as ZP, revealing that MQD deposition does not contribute to the substantial increase in the specific surface area. As displayed in Fig. 1g, three peaks at 248, 308 and 343 cm^{-1} are clearly seen in the Raman spectra of ZIS, ZP and ZPM, which can be assigned to the longitudinal optical mode (LO_1), transverse optical mode (TO_2), and longitudinal optical mode (LO_2) of ZIS, respectively.[38,39] Analogous to the XRD results, no diffraction peak attributable to PDDA and MQDs is observed in the Raman results of ZPM. Nevertheless, decreased peak intensity is obviously seen in the Raman spectra of ZP and ZPM compared with that of ZIS, verifying the seamless PDDA encapsulation and electrostatic deposition of MQDs on the ZIS surface, thereby shielding the ZIS peaks.

XPS was utilized to gain composition and elemental chemical valence states of the samples. As shown in Fig. S8,† the survey spectrum of ZPM is similar to that of the blank ZIS with the presence of Zn, In, S and C elements, but N and Ti signals are hard to detect in the survey spectrum of ZPM, and this is probably due to the low loading amount of PDDA and MQDs. As reflected by the high-resolution Zn 2p spectra of ZPM, two peaks at 1022.07 (Zn $2p_{3/2}$) and 1045.27 (Zn $2p_{1/2}$) eV are attributable to the Zn^{2+} species,[31,32] which agrees with the high-resolution Zn 2p spectrum of ZIS (Fig. 1h). Also, as revealed in Fig. 1iII, the high-resolution In 3d spectrum of ZPM with two peaks at 445.35 (In $2p_{5/2}$) and 452.46 (In $2p_{3/2}$) eV is ascribed to the In^{3+} species,[31,32] which is consistent with the high-resolution In 3d spectra of ZIS (Fig. 1iI). Fig. 1jII shows the high-resolution S 2p spectrum of ZPM in which two doublet peaks at 161.96 (S $2p_{1/2}$) and 163.17 (S $2p_{3/2}$) eV correspond to the S element in the −2 reduction state, which is consistent with the high-resolution S spectrum of ZIS (Fig. 1jI).[31,40] Fig. 1k shows the high-resolution C 1s spectra of ZIS and ZPM, in which the peak at 284.8 eV is assigned to the C–C & C–H species, and the second peak at 286.66 eV is assigned to C–N, while the third peak at 288.31 eV is attributed to the C=O species from residual thioacetamide (TAA) molecules coated on the ZIS surface.[31,41] Notably, ZIS and ZPM demonstrate almost the same high-resolution Zn 2p, In 3d, S 2p, and C 1s spectra with the same B.E. position, implying that seamless PDDA encapsulation and electrostatic deposition of MQDs on the ZIS surface do not alter the elemental chemical states of the ZIS substrate. Besides, the high-resolution N spectrum of ZPM (Fig. 1m) demonstrates two peaks at 400.14 and 402.59 eV, which are assigned to the primary amine from TAA and NH_4^+ from the PDDA layer,[31,42] respectively. This is distinct from the high-resolution N1s spectrum of pristine ZIS (Fig. 1l). Fig. S9† shows the high-resolution Ti 2p spectrum of ZPM, wherein a rather weak Ti signal is observed, and it is mainly caused by the low loading amount of MQDs.[16] For comparison, B.E. *vs.* chemical bond species for the different samples is summarized in Table S3.†

Morphology and textural structure of the samples were disclosed by FESEM and TEM measurements. Fig. 2(a and b) show that the blank ZIS NS substrate exhibits a uniform sheet-like structure, wherein ZIS NSs with a size of 100–150nm are randomly stacked with each other. EDS analysis of the SEM image shows the presence of Zn, In and S signals (Fig. S10†), which further proves the successful preparation of ZIS NSs. Fig. 2c shows the HRTEM image of ZIS NSs, in which the lattice fringe of *ca.* 0.33 nm is assigned to the (100) crystallographic plane of $ZnIn_2S_4$. The selected area electron diffraction (SAED) pattern of ZIS (inset, Fig. 2c) demonstrates the characteristic (110) and (100) crystal planes of ZIS, revealing the high crystallinity of ZIS NSs, and this is in line with the XRD results. As displayed in Fig. S11,† ZP still demonstrates the flat 2D nanosheet structure after ultra-thin PDDA encapsulation. The SEM elemental mapping result of ZP reveals the appearance of C, N and Cl signals, strongly proving the attachment of PDDA on the ZIS surface. Fig. S12† shows the FESEM image of ZPM, which reveals that the 2D nanoarchitecture of the ZIS NS matrix is retained after ultrathin PDDA and MQDs are evenly deposited on the ZIS substrate *via* electrostatic self-assembly. HRTEM images of ZPM are displayed in Fig. 2(d and e) and S13,† which confirm uniform encapsulation of ZIS with an ultra-thin PDDA layer on the surface. Furthermore, MQDs are randomly distributed on the 2D framework of PDDA-modified ZIS with intimate contact, as marked by the yellow circles. For reference, the original image of Fig. 2d is provided in Fig. S14.† The lattice

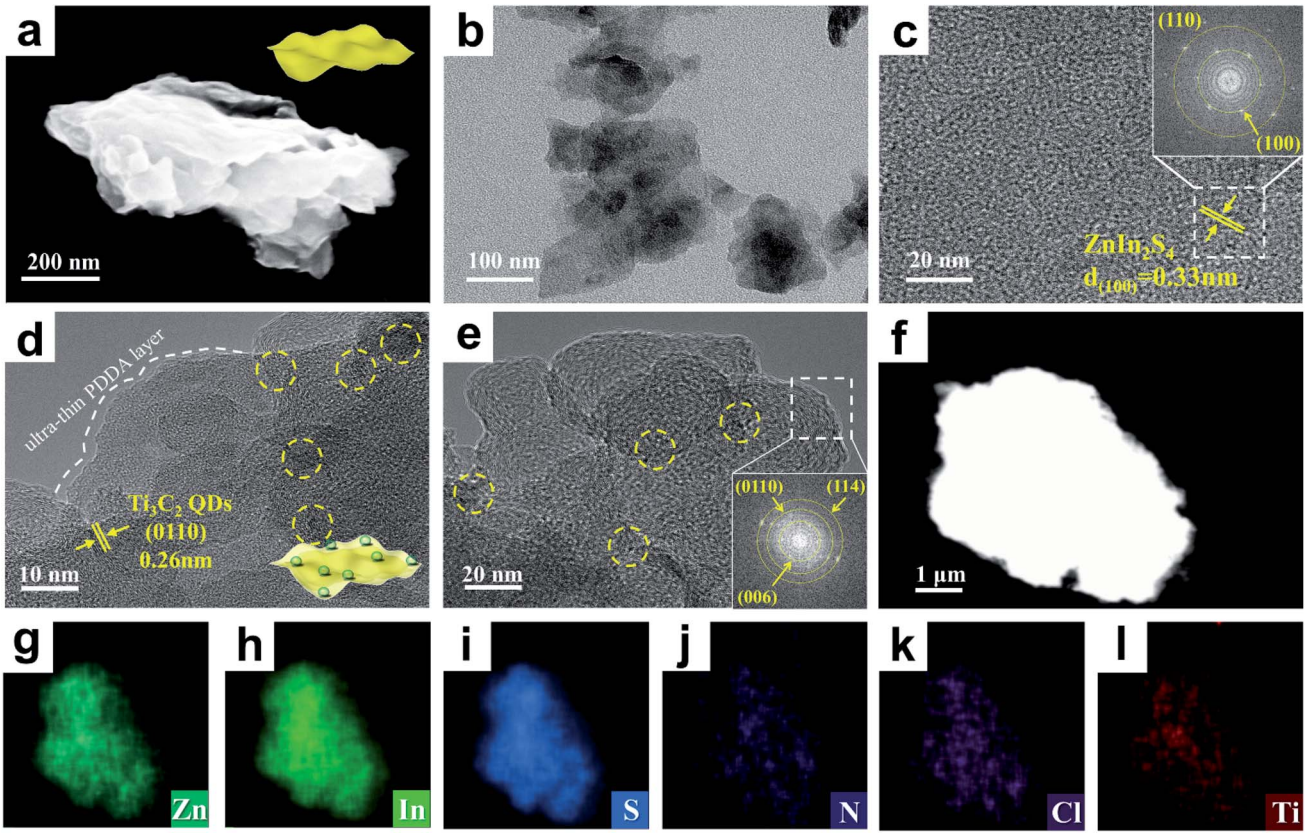

Fig. 2 (a) FESEM, (b) TEM and (c) HRTEM images of ZIS NSs with the schematic model and SAED pattern in the insets; (d & e) HRTEM images with the schematic model and SAED pattern in the insets, and (f) TEM image of ZPM with elemental mapping results for (g) Zn, (h) In, (i) S, (j) N, (k) Cl, and (l) Ti signals.

fringe of 0.26 nm (Fig. 2d) in the HRTEM image of ZPM is attributable to the (0110) crystallographic plane of Ti_3C_2 QDs (MQDs), and the SAED pattern of ZPM (inset, Fig. 2e) verifies the characteristic (114) and (006) crystal planes of ZIS and the (0110) crystal plane of MQDs. Consistently, as displayed in Fig. 2(f–l), homogeneous distribution patterns of Zn, In, S, N, Cl and Ti elements in ZPM are revealed by the elemental mapping result, among which the Ti signal arises from the MQDs and Cl & N from the PDDA layer, once again confirming the successful self-assembly of MQDs and the PDDA layer on the ZIS NSs.

3.2 Photocatalytic performances

Photoactivities of the samples were evaluated by anaerobic reduction of 4-nitroaniline (4-NA) to 4-phenylenediamine (4-PDA) under visible light irradiation (λ > 420 nm) with the addition of sodium sulfite as the hole scavenger and N_2 bubbling under ambient conditions, which makes electrons the only active species during the reaction. Specifically, Fig. S15† shows the UV-vis absorption spectra of 4-NA in the presence of ZPM under visible light irradiation, wherein the peak intensity at 380 nm corresponding to 4-NA gradually decreases, and meanwhile, the peak intensity at 320 nm corresponding to 4-PDA gradually increases, indicating successful photoreduction of 4-NA to 4-PDA. As shown in Fig. S16,† 4-NA was not reduced in the absence of the catalyst or light irradiation, indicating that the reaction is indeed driven by a photocatalytic process. As mirrored in Fig. S17a,† the photoactivity of ZP toward anaerobic photoreduction of 4-NA to 4-PDA is closely associated with the PDDA concentration, that is, the photoactivity of ZP remarkably increases when increasing the PDDA concentration to 10 mg mL^{-1}, and then it gradually decreases upon further increasing the concentration to 20 mg mL^{-1}. However, it should be noted that photoactivities of all these ZP-(5, 10, 15, 20) samples always markedly exceed that of pure ZIS, which verifies the important role of the PDDA layer in boosting the photoactivity of ZP. The decreased conversion of ZP when the PDDA concentration exceeds 10 mg mL^{-1} is ascribed to the fact that light absorption of the ZIS substrate is shielded by the thick PDDA encapsulation that might increase the interfacial charge transfer resistance, thus leading to the inferior photoactivity. Hence, the optimal PDDA concentration is determined to be 10 mg mL^{-1}, based on which we explored the deposition amount of MQDs on the photoactive ZP-10 NSs. As shown in Fig. S17b,† photoactivities of ZPM nanocomposites increase with increasing volume of the MQD aqueous solution added into the reaction system from 5 to 10 mL, and then gradually decrease upon further increasing the volume to 20 mL. The photoactivity of the optimal ZPM-10 sample (PDDA: 10 mg mL^{-1}; MQDs:10 mL) is approximately 4.5 times larger than that of pure ZIS and 2.3 times larger than that of ZP-10,

which is attributed to the improved charge separation afforded by MQDs and close interfacial interaction endowed by electrostatic self-assembly. Thus, ZPM-10 is selected as the optimal sample for the following systematic comparison. In addition, a series of controlled experiments were performed to verify the role of the PDDA layer and MQDs in ZPM heterostructured photosystems. As shown in Fig. S18,† pure PDDA and MQDs do not show photoactivities toward 4-NA reduction, suggesting that ZIS is the only source for producing photoinduced charge carriers. Thus, we certify that PDDA and MQDs themselves do not generate electrons but rather serve as carrier transport media, which facilitates the construction of a continuous charge transfer channel over ZIS NSs to synergistically enhance the photoreduction performance of the ZPM nanocomposite.

To highlight the pivotal role of the PDDA layer in constructing a continuous charge transfer channel and boosting the photoactivity of ZPM, a ZIS/MQD (ZM) nanocomposite counterpart without PDDA encapsulation was prepared with its photoactivity probed. As shown in Fig. S19a,† the FTIR spectrum of ZM confirms that MQDs have been successfully loaded on the ZIS NSs, and the XRD pattern of ZM (Fig. S19b†) corresponds to the hexagonal phase $ZnIn_2S_4$, suggesting that MQD deposition does not alter the crystal structure of the ZIS substrate. Moreover, SEM images manifest that ZM still shows a 2D nanosheet structure (Fig. S19c & d†). As shown in Fig. 3a, the photoactivity of ZIS toward 4-NA reduction is much lower than that of ZP, and moreover, the photoactivity of ZM is markedly lower than that of ZPM, concurrently verifying that the PDDA coating is critical to accelerate the interfacial charge transfer efficiency. The enhanced photoactivity of ZM relative to that of ZIS strongly implies the crucial role of MQDs as a carrier mediator to boost the charge separation and transfer. The photoactivities of the samples follow the order of ZPM>ZP≈ZM>ZIS. With a view to ascertaining the general photoactivities of the ZPM photosystems, a series of nitroaromatics including 2-nitroaniline (2-NA), 4-nitrophenol (4-NP), 2-nitrophenol (2-NP), 1-bromo-4-nitrobenzene, 1-chloro-4-nitrobenzene, 4-nitrotoluene, 4-nitroanisole, and nitrobenzene were also utilized as the reactants for photocatalysis. As displayed in Fig. 3b–i, analogous boosted photoactivities are visualized over ZPM relative to those of ZIS, ZP and ZM under the same conditions, and they follow a similar trend, signifying the versatile photoactivities of ZPM and general roles of PDDA and MQDs in boosting the photoactivity. For comparison, the photocatalytic conversion efficiency of the different samples toward reduction of nitroaromatic compounds is summarized in Table S4.† Moreover, a similar result is seen in photocatalytic hydrogen generation performances of ZIS, ZP, ZPM and ZM (Fig. 3j). More specifically, the photocatalytic hydrogen generation rate of ZPM is *ca.* 1.8 and 1.3 times as high as those of pure ZIS and ZP, and reaches 0.19 mmol h^{-1} g^{-1}, which corresponds to the AQY of *ca.* 0.4% at 450 nm (Fig. S20†).

The crucial role of electrons in boosting the selective photoreduction catalysis is verified by adding $AgNO_3$ into the reaction system as an electron scavenger. Fig. 4a shows that the photocatalytic performance of ZPM toward 4-NA reduction is drastically decreased when $AgNO_3$ was added into the reaction system, indicating that electrons indeed play an unshakable role in initiating selective photoreduction reactions. Furthermore, a control experiment without adding a hole scavenger into the reaction system was also performed (Fig. S21†). The result manifests that the photocatalytic performance of ZPM decreases sharply without adding a hole scavenger, suggesting that the presence of holes accelerates the recombination of electron–hole pairs and thus reduces the photoreduction efficiency. As shown in Fig. 4b, the ZPM nanocomposite demonstrates good photostability with tiny photoactivity decay after five successive cycling reactions. Fig. S22a† shows the XRD patterns of ZPM after cycling reactions, which unveils the same crystal structure as that of pristine ZPM, indicating that the crystal structure of the catalyst is not changed after the cycling reactions. Moreover, Fig. S22(b–i)† show the SEM images and elemental mapping results of ZPM after cycling reactions, and the results indicate that ZPM still demonstrates the 2D sheet structure with each element signal retained after cycling reactions. The results corroborate that ZPM is a robust and stable photocatalyst. In addition, the active wavelength region responsible for the enhanced photoactivities of ZPM was determined by probing the action spectrum of ZPM under different monochromatic light irradiation. A substantial peak ranging from 400 to 600 nm is seen in the action spectrum (Fig. 4c) and S.T.H result (Fig. 4d) of ZPM toward either photoreduction of 4-NA or photocatalytic hydrogen evolution, which confirms the substantial light harvesting capability of the ZIS substrate in boosting the photoactivities of ZPM. Besides, photoactivities of ZPM under different light intensities indicate that the hydrogen evolution rate is closely related to the light intensity (Fig. 4e). As shown in Fig. 4f, the influence of the sacrificial reagent on the photocatalytic hydrogen evolution performance of ZPM was further probed, for which Na_2S/Na_2SO_3 demonstrates the optimal solar-to-hydrogen conversion efficiency.

PDDA-encapsulated ZIS was replaced with other positively charged non-conductive polymers or small organic molecules [(*e.g.* branched polyethylenimine (BPEI), poly(allylamine hydrochloride) (PAH), 2-aminoethanethiol (AET) and 3-aminopropyl-trimethoxysilane (APTES)] to reveal the universality of forming a continuous charge transfer channel over ZIS/MQD-based photosystems. Molecular structures of these surface modification mediums are exhibited in Fig. S23.† Compared with the original negatively charged ZIS substrate, ZIS/BPEI (+16.0 mV), ZIS/PAH (+3.99 mV), ZIS/AET (+10.6 mV) and ZIS/APTES (+25.8 mV) demonstrated positively charged surfaces (Fig. S24†), implying their surface charge reversal after polymer modification. Thus, these positively charged substrates can also undergo analogous electrostatic self-assembly with the negatively charged MQDs. Detailed characterization of the ZIS/BPEI/MQD, ZIS/PAH/MQD, ZIS/AET/MQD and ZIS/APTES/MQD heterostructures is provided in Fig. S(25–28),† which confirms the deposition of MQDs on the ZIS substrate from the perspectives of crystalline structure, optical properties, microscopic morphology and elemental composition. Photocatalytic performances of these heterostructures toward 4-NA reduction and hydrogen evolution are probed to evaluate the general role

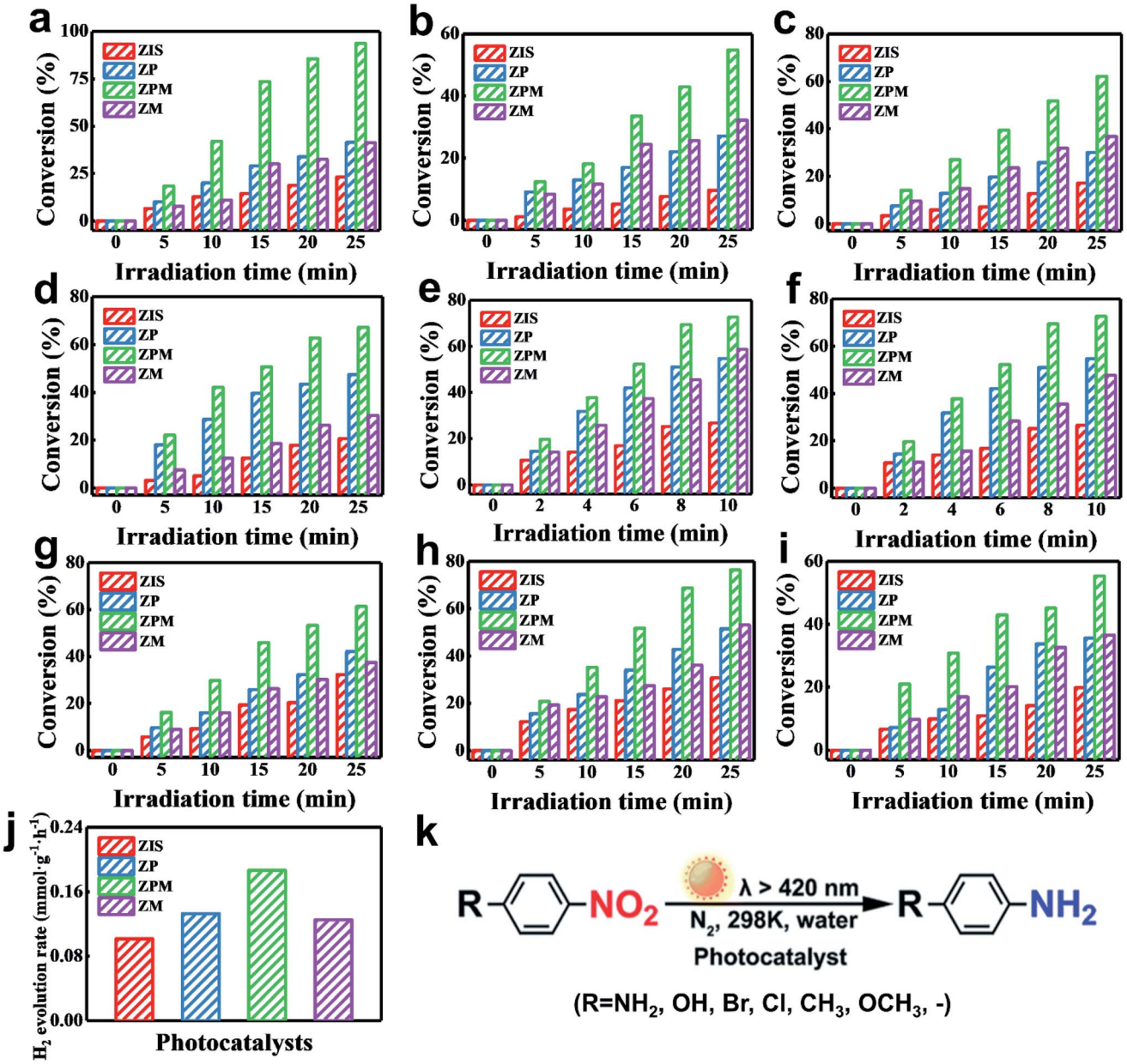

Fig. 3 Photoactivities of ZIS, ZP, ZPM and ZM toward photocatalytic reduction of aromatic nitro compounds including (a) 4-NA, (b) 2-NA, (c) 4-NP, (d) 2-NP, (e) 1-bromo-4-nitrobenzene, (f) 1-chloro-4-nitrobenzene, (g) 4-nitrotoluene, (h) 4-nitroanisole, and (i) nitrobenzene with the addition of sodium sulfite as the hole scavenger and N_2 bubbling under ambient conditions and visible light irradiation ($\lambda > 420$ nm) along with the corresponding (k) reaction model. (j) Photocatalytic hydrogen evolution performances of ZIS, ZP, ZPM and ZM under visible light irradiation ($\lambda >$ 420 nm).

of such continuous charge transfer channels constructed over ZIS/MQD-based photosystems. As displayed in Fig. 5a–d&h, these ternary heterostructures always show significantly enhanced photocatalytic performances relative to those of the corresponding binary counterparts and pure ZIS NSs under identical experimental conditions, implying the general role of surface charge modification reagents in facilitating a charge transfer cascade afforded by MQDs. On the other hand, TMC NS (TMCs: CdS, CIS, and IS) substrates are utilized to replace ZIS NSs to probe the influence of the semiconductor matrix on the charge transfer efficiency. Zeta potentials of TMC/PDDA (Fig. S29†) nanocomposites make them applicable building blocks for analogous electrostatic self-assembly with MQDs. Structural characterization of TMCs/PDDA/MQDs is provided in Fig. S(30–32).† Note that similar photoactivity enhancement is observed over TMCs/PDDA/MQDs compared with those of pure TMC and TMC/PDDA counterparts [Fig. 5e–g&i)] toward photoreduction of 4-NA and hydrogen evolution. For comparison, the photocatalytic conversion efficiency of the different samples toward 4-NA photoreduction is summarized in Table S5.† The above results strongly confirm that the cascade charge

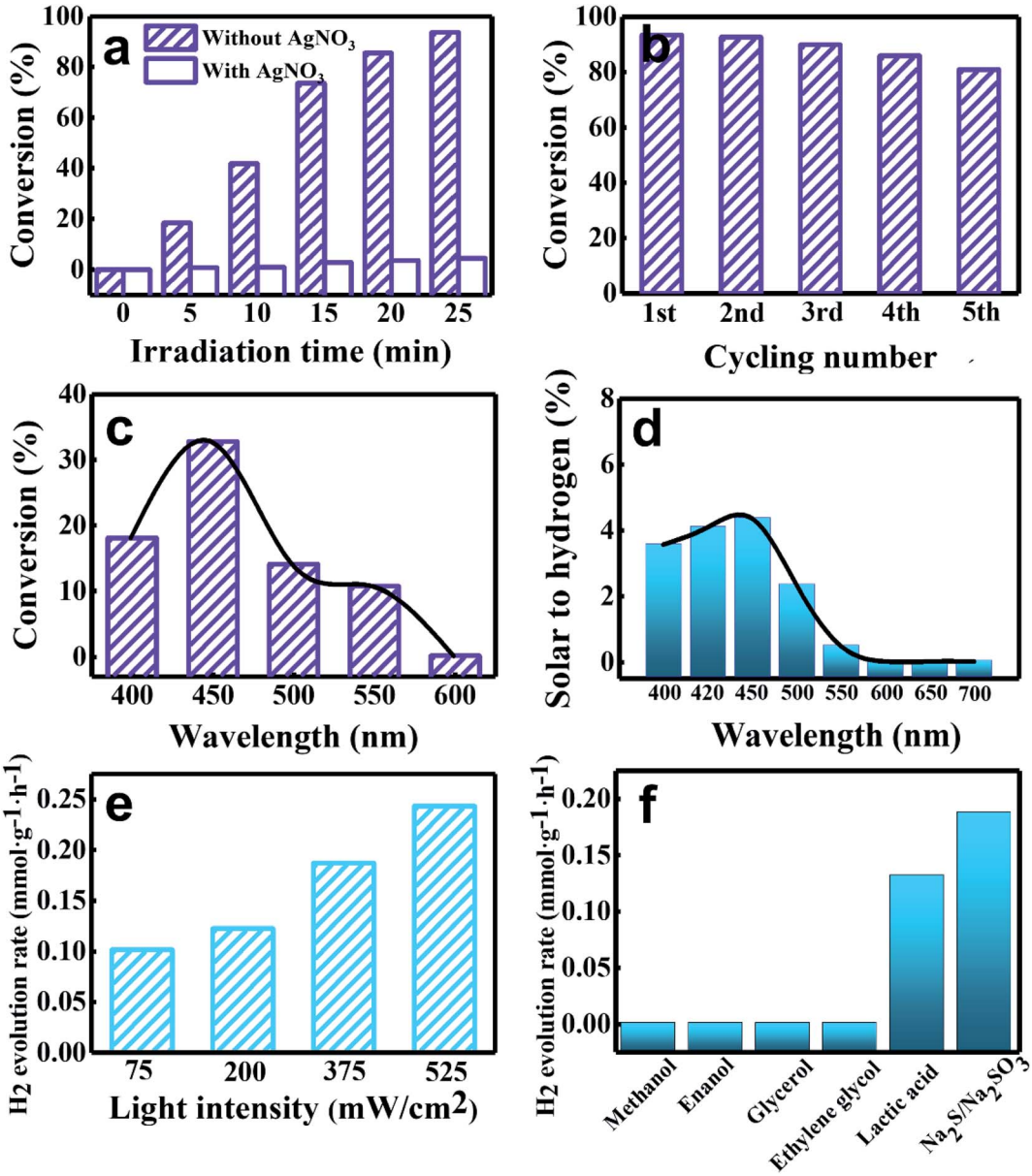

Fig. 4 (a) Photoactivities of ZPM towards 4-NA reduction with and without addition of $AgNO_3$ as an electron scavenger; (b) cycling reactions of ZPM; (c) action spectrum for photoreduction of 4-NA over ZPM under different monochromatic light irradiation; (d) S.T.H conversion efficiency of ZPM under monochromatic light irradiation; photocatalytic hydrogen evolution rates of ZPM (e) under different light intensities and (f) utilizing different sacrificial reagents.

transfer mechanism is general and it is not confined to the category of TMCs and the surface-modifying medium.

3.3 PEC performances

PEC analysis was carried out to evaluate the separation efficiency of photoinduced electron–hole pairs over the different samples. Electrochemical impedance spectroscopy (EIS) was utilized to probe the charge transfer resistance in the interfacial region of the working electrode and electrolyte. Fig. 6a manifests that ZPM exhibits the smallest semicircular arc radius under visible light irradiation compared with ZIS and ZP counterparts, which verifies that ZPM exhibits the smallest charge transfer resistance and the optimal charge separation efficiency, followed successively by ZP and ZIS. This result suggests that charge separation over ZPM is much more efficient than those over single and binary counterparts, which is attributed to the *in situ* generation of continuous charge transfer channels concurrently provided by the PDDA layer and MQDs, thereby facilitating effective charge separation and transfer. Consistently, simulated EIS results are summarized in Table S6,† wherein ZPM (5202 ohm) exhibits a smaller charge resistance (R_{ct}) under visible light irradiation than those of ZIS (9187 ohm) and ZP (7365 ohm). The Mott–Schottky (M–S) plot is utilized to measure the carrier density of the photoelectrodes.

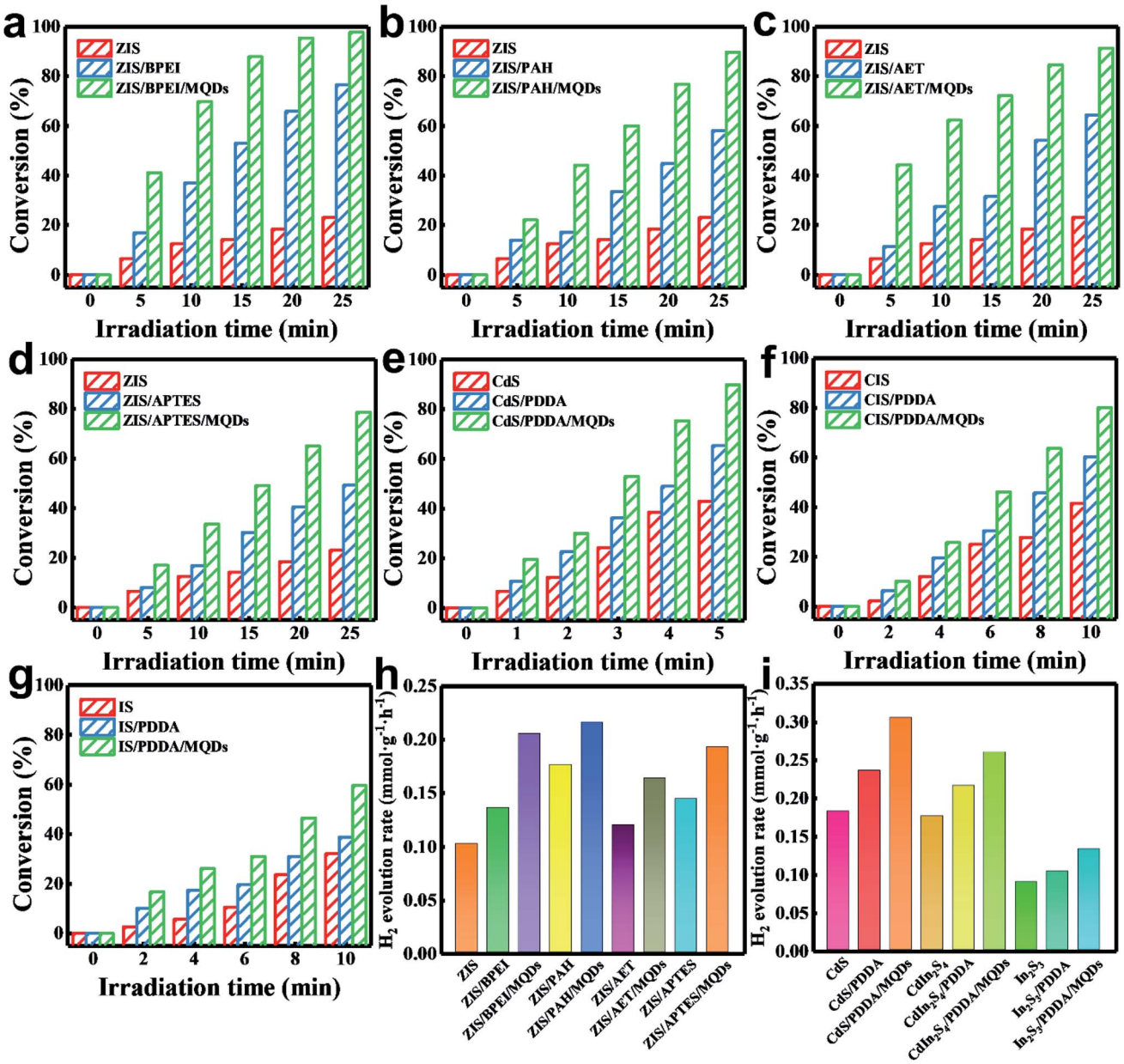

Fig. 5 Photoactivities of (a) blank ZIS, ZIS/BPEI and ZIS/BPEI/MQD, (b) ZIS, ZIS/PAH and ZIS/PAH/MQD, and (c) ZIS, ZIS/AET and ZIS/AET/MQD; (d) ZIS, ZIS/APTES and ZIS/APTES/MQD, (e) CdS, CdS/PDDA and CdS/PDDA/MQD, (f) CIS, CIS/PDDA and CIS/PDDA/MQD, and (g) IS, IS/PDDA and IS/PDDA/MQD heterostructures toward 4-NA reduction with addition of sodium sulfite as the hole scavenger and N_2 bubbling under ambient conditions and visible light irradiation (λ > 420 nm). Photocatalytic H_2 generation performances of (h) ZIS, (ZIS/BPEI and ZIS/BPEI/MQDs), (ZIS/PAH and ZIS/PAH/MQDs), (ZIS/AET and ZIS/AET/MQDs), (ZIS/APTES and ZIS/APTES/MQDs), and (i) (CdS, CdS/PDDA, and CdS/PDDA/MQDs), (CIS, CIS/PDDA, and CIS/PDDA/MQDs), and (IS, IS/PDDA, and IS/PDDA/MQDs) under visible light irradiation (λ > 420 nm).

As displayed in Fig. 6b, ZPM shows the smallest linear slope compared with ZIS and ZP, which implies that ZPM demonstrates the largest carrier density among these three samples. Moreover, the charge carrier density (N_D) of the electrodes can be calculated using the following equation:

$$N_D = \left(\frac{2}{\varepsilon_r \varepsilon_0 e_0}\right)\left[\frac{d\left(\frac{1}{C^2}\right)}{dV}\right]^{-1}$$

where ε_r denotes the dielectric constant of the semiconductor (ε_{ZIS}= 4.73),[31] ε_0 denotes the vacuum permittivity (8.86×10^{-12} Fm^{-1}), e_0 is the electronic charge unit (1.6×10^{-19} C), and V is the potential applied to the electrode. As shown in Fig. 6c, charge carrier densities (N_D) of ZIS, ZP and ZPM are determined to be 4.97×10^{19}, 6.32×10^{19} and 10.27×10^{19}, respectively. Apparently, ZPM demonstrates the largest N_D followed in turn by ZP and ZIS. Fig. 6d shows the open circuit voltage decay (OCVD) results of ZIS, ZP and ZPM, in which ZPM shows a larger

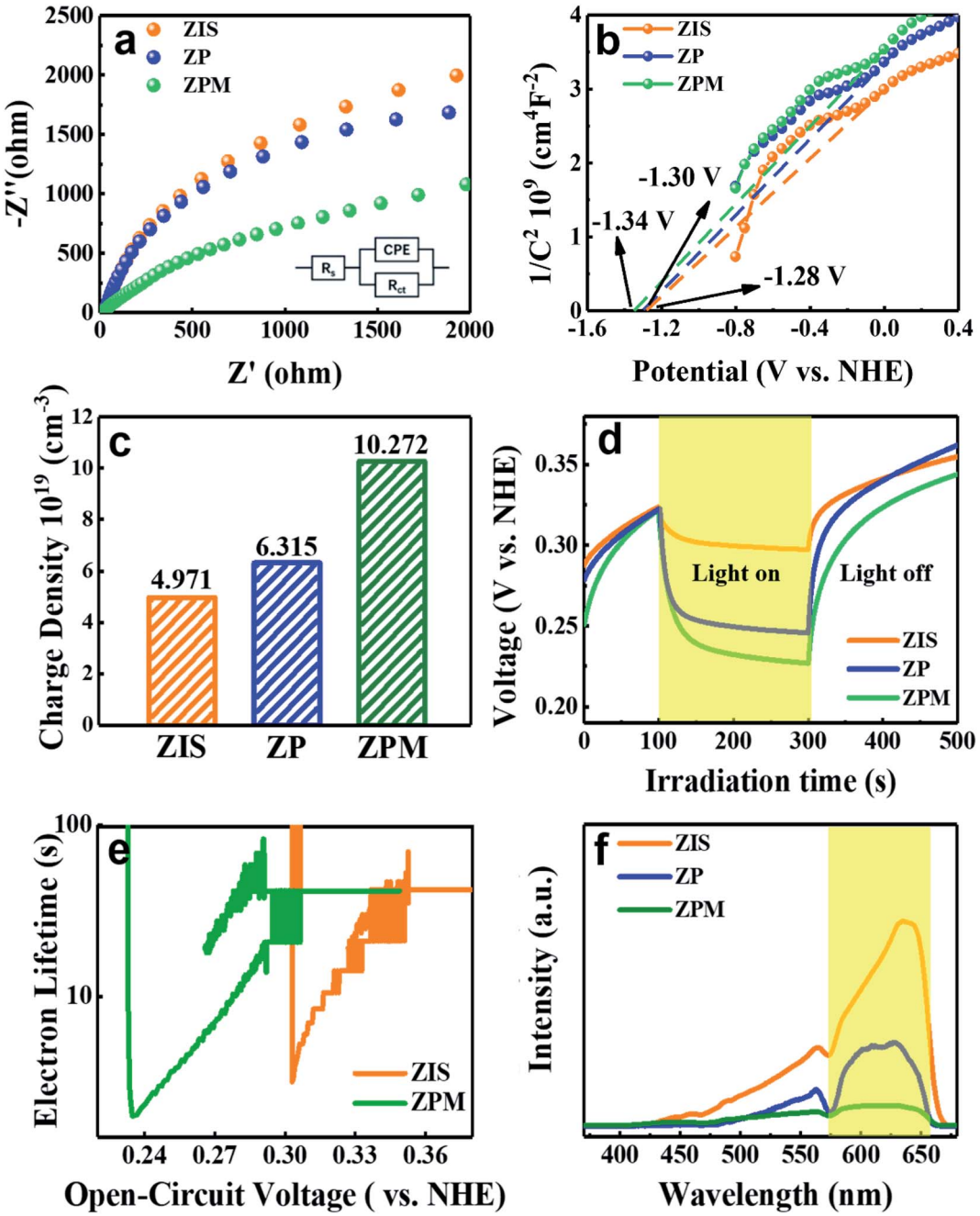

Fig. 6 (a) EIS Nyquist plots, (b) Mott–Schottky plots, (c) charge carrier densities, (d) open-circuit potential decay (OCVD), and (e) electron lifetimes of ZIS, ZP and ZPM under visible light irradiation ($\lambda > 420$ nm). The inset in (a) demonstrates the equivalent circuit. (f) PL spectra of ZIS, ZP and ZPM ($\lambda_{ex} = 350$ nm).

photovoltage and longer electron lifetime (Fig. 6e) than ZP and ZPM, confirming that ZPM exhibits the most efficient charge separation among these samples. The photoluminescence (PL) technique was utilized to evaluate the charge separation efficiency of the ZPM photosystem. As unveiled in Fig. 6f, the PL intensity of ZPM is much lower than those of ZP and ZIS, suggesting that charge recombination over ZPM is greatly inhibited by intimate PDDA encapsulation and MQD deposition. It is noteworthy that PEC and PL results are in good agreement with the photocatalytic performances.

3.4 Photocatalytic mechanism

Fig. 6b and S(33–35)† show the M–S plots of ZIS, ZP and ZPM, by which flat-band potentials (V_{fb}) are determined to be *ca.* −1.28 V, −1.30 V and −1.34 V *vs.* the normal hydrogen electrode (NHE). Notably, the V_{fb} of ZIS is not altered by PDDA encapsulation and MQD deposition. According to the formula $E_g = V_{VB} - V_{CB}$, the valence band potential (V_{VB}) of ZIS is calculated to be 0.78 V *vs.* NHE, wherein the E_g value (2.06 eV) is determined by the DRS result (Fig. 1d). According to the

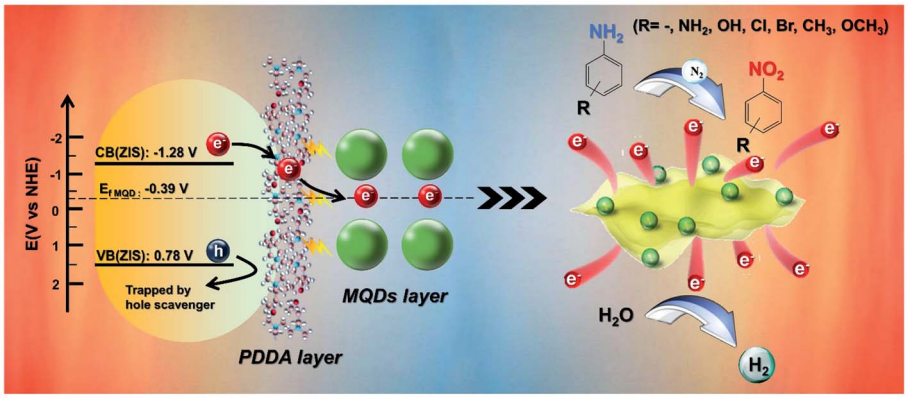

Scheme 1 Schematic illustration of the photocatalytic mechanism of ZPM.

previous work,[36] the E_f of MQDs is located at *ca.* −0.39 eV *vs.* NHE. Consequently, the result verifies that the potential difference between the CB of ZIS and E_f of MQDs provides sufficient dynamic impetus to surmount the energy barrier for electron transfer. The photocatalytic mechanism of ZPM nanocomposites is thus proposed and depicted in Scheme 1. Specifically, ZIS is photoexcited under visible light irradiation to produce electron–hole pairs with electrons photoexcited to the CB, leaving holes in the VB. Subsequently, the ultra-thin PDDA layer evenly coated on the surface of ZIS acts as an efficient electron relay medium to accelerate electron migration. The photoelectrons then rapidly migrate to the neighboring MQD layer as a result of intimate interfacial contact and favorable energy level alignment with the ZIS substrate, thus effectively retarding the charge recombination and prolonging the charge lifetime over ZIS NSs. Electrons that go through the ultra-thin intermediate PDDA layer and MQD layer are involved in the photoreduction of aromatic nitro compounds to the corresponding amino derivatives, wherein N_2 bubbling and addition of a hole scavenger (Na_2SO_3) were carried out in the reaction system to ensure that the photoelectron is the only active species. Besides, electrons ultimately captured by MQDs can also efficiently reduce the protons to hydrogen owing to the synergistic effect of PDDA encapsulation and MQD deposition on boosting the charge separation.

4. Conclusions

In summary, an efficient, facile and general electrostatic self-assembly strategy was presented to elaborately construct TMCs/PDDA/MQD (TMCs: ZIS, CdS, CIS, and IS) photosystems with continuous charge transfer channels for visible-light-driven selective photoreduction of nitroaromatics to amino aromatics and hydrogen generation. The solid-state ultrathin non-conjugated PDDA interim layer demonstrates an unexpected electron-withdrawing ability to relay unidirectional electron flow from TMCs to MQDs. The MQDs attached on the surface of PDDA-encapsulated TMCs serve as electron traps to further accelerate electron transfer, leading to a directional charge transfer cascade and prolonging the charge lifetime of TMCs. Furthermore, we ascertain that the concept of cascade charge regulation over TMCs/polymer/MQD multilayered heterostructures is universal. Our work would open a new vista for fine tuning of charge separation over TMC NSs *via* non-conjugated insulating polymers for solar energy conversion.

Data availability

The data supporting the findings of this study are included in the main text and in the ESI file.†

Author contributions

Fang-Xing Xiao contributed to the conception of the study, designed the method, supervised and directed the experiments, reviewed and revised the manuscript. Bi-Jian Liu performed the experiments, analyzed the data and wrote the manuscript. Hao Liang, Qiao-Ling Mo, Shen Li, Bo Tang and Shi-Cheng Zhu helped perform the analysis with constructive discussions.

Conflicts of interest

There are no conflicts to declare.

Acknowledgements

The support by the Award Program for Minjiang scholar professorship is greatly acknowledged. This work was financially supported by the National Natural Science Foundation of China (No. 21703038 and 22072025) and Fujian Science & Technology Innovation Laboratory for Optoelectronic Information of China (2021ZR147).

References

1 S. Kohtani, A. Kawashima and H. Miyabe, *Front. Chem.*, 2019, 7, 630.
2 F. X. Xiao, M. Pagliaro, Y. J. Xu and B. Liu, *Chem. Soc. Rev.*, 2016, **45**, 3088–3121.
3 F. Haque, T. Daeneke, K. Kalantar-zadeh and J. Z. Ou, *Nano-Micro Lett.*, 2018, **10**, 1–27.

4 J. H. Han, M. Kwak, Y. Kim and J. Cheon, *Chem. Rev.*, 2018, **118**, 6151–6188.
5 K. Kalantar-zadeh, J. Z. Ou, T. Daeneke, A. Mitchell, T. Sasaki and M. S. Fuhrer, *Appl. Mater. Today*, 2016, **5**, 73–89.
6 D. Jiang, Q. Zhang, D. Chen, B. Wen, Q. Song, C. Zhou and D. Li, *J. Alloys Compd.*, 2021, **865**, 158836.
7 Q. Zhu, Y. Sun, S. Xu, Y. Li, X. Lin and Y. Qin, *J. Hazard. Mater.*, 2020, **382**, 121098.
8 A. Uddin, T. Muhmood, Z. Guo, J. Gu, H. Chen and F. Jiang, *J. Alloys Compd.*, 2020, **845**, 156206.
9 J. Singh, R. S. Kumar and R. K. Soni, *J. Alloys Compd.*, 2020, **849**, 156502.
10 R. Bera, S. Kundu and A. Patra, *ACS Appl. Mater. Interfaces*, 2015, **7**, 13251–13259.
11 S. J. A. Moniz, S. A. Shevlin, D. J. Martin, Z. X. Guo and J. W. Tang, *Energy Environ. Sci.*, 2015, **8**, 731–759.
12 L. X. Meng, D. W. Rao, W. Tian, F. R. Cao, X. H. Yan and L. Li, *Angew. Chem., Int. Ed.*, 2018, **57**, 16882–16887.
13 P. T. Liu, Y. G. Liu, W. C. Ye, J. Ma and D. Q. Gao, *Nanotechnology*, 2016, **27**, 25403.
14 Y. J. Yuan, H. W. Lu, Z. G. Ji, J. S. Zhong, M. Y. Ding, D. Q. Chen, Y. H. Li, W. G. Tu, D. P. Cao, Z. T. Yu and Z. G. Zou, *Chem. Eng. J.*, 2015, **275**, 8–16.
15 L. Ge, C. C. Han, X. L. Xiao and L. L. Guo, *Int. J. Hydrogen Energy*, 2013, **38**, 6960–6969.
16 H. J. Lin, Q. L. Mo, S. Xu, Z. Q. Wei, X. Y. Fu, X. Lin and F. X. Xiao, *J. Catal.*, 2020, **391**, 485–496.
17 X. Q. Xie, N. Zhang, Z. R. Tang, M. Anpo and Y.-J. Xu, *Appl. Catal., B*, 2018, **237**, 43–49.
18 Q. Xue, H. J. Zhang, M. S. Zhu, Z. X. Pei, H. F. Li, Z. F. Wang, Y. Huang, Y. Huang, Q. H. Deng, J. Zhou, S. Y. Du, Q. Huang and C. Y. Zhi, *Adv. Mater.*, 2017, **29**, 1604847.
19 B. B. Shao, Z. F. Liu, G. M. Zeng, H. Wang, Q. H. Liang, Q. Y. He, M. Cheng, C. Y. Zhou, L. B. Jiang and B. Song, *J. Mater. Chem. A*, 2020, **8**, 7508–7535.
20 Z. P. Zeng, Y. B. Yan, J. Chen, P. Zan, Q. H. Tian and P. Chen, *Adv. Funct. Mater.*, 2019, **29**, 1806500.
21 Y. J. Li, L. Ding, Y. C. Guo, Z. Q. Liang, H. Z. Cui and J. Tian, *ACS Appl. Mater. Interfaces*, 2019, **11**, 41440–41447.
22 X. Li, C. Liu and B. van der Bruggen, *J. Mater. Chem. A*, 2020, **8**, 20870–20896.
23 W. N. Xu, P. A. Ledin, V. V. Shevchenko and V. V. Tsukruk, *ACS Appl. Mater. Interfaces*, 2015, **7**, 12570–12596.
24 Z. Q. Wei, S. Hou, X. Lin, S. Xu, X. C. Dai, Y. H. Li, J. Y. Li, F.-X. Xiao and Y.-J. Xu, *J. Am. Chem. Soc.*, 2020, **142**, 21899–21912.
25 H. J. Lin, S. Xu, X. Y. Fu, Z. Q. Wei, M. H. Huang, X. Lin, Y. H. He, G. C. Xiao and F.-X. Xiao, *Inorg. Chem.*, 2020, **59**, 4129–4139.
26 Y. B. Li, T. Li, X. C. Dai, M. H. Huang, S. Hou, X. Y. Fu, Z. Q. Wei, Y. H. He, G. C. Xiao and F.-X. Xiao, *ACS Appl. Mater. Interfaces*, 2020, **12**, 4373–4384.
27 S. Hou, M. H. Huang, Y. B. Li, S. Xu, X. Lin, X. Y. Fu and F.-X. Xiao, *Inorg. Chem.*, 2020, **59**, 16654–16664.
28 S. Xu, M. H. Huang, T. Li, Z. Q. Wei, X. Li, X. C. Dai, S. Hou, X. Y. Fu and F.-X. Xiao, *J. Mater. Chem. A*, 2020, **8**, 8360–8375.
29 R. S. Jing, J. S. Yang, S. T. Li, S. F. Zhao, P. F. Wang, Y. Y. Liu, A. J. Liu, Z. L. Meng, H. W. Huang, Z. L. Zhang and Q. Zhang, *J. Colloid Interface Sci.*, 2020, **576**, 34–46.
30 Q. Zhang, Q. An, X. L. Luan, H. W. Huang, X. W. Li, Z. L. Meng, W. S. Tong, X. D. Chen, P. K. Chu and Y. H. Zhang, *Nanoscale*, 2015, **7**, 14002–14009.
31 Q. L. Mo, X. Lin, Z. Q. Wei, X. C. Dai, S. Hou, T. Li and F.-X. Xiao, *J. Mater. Chem. A*, 2020, **8**, 16392–16404.
32 M. Q. Yang, Y. J. Xu, W. H. Lu, K. Y. Zeng, H. Zhu, Q. H. Xu and G. W. Ho, *Nat. Commun.*, 2017, **8**, 14224.
33 X. Y. Fu, Z. Q. Wei, S. Xu, X. Lin, S. Hou and F. X. Xiao, *J. Phys. Chem. Lett.*, 2020, **11**, 9138–9143.
34 X. Y. Fu, Y. B. Li, M. H. Huang, T. Li, X. C. Dai, S. Hou, Z. Q. Wei and F. X. Xiao, *Inorg. Chem.*, 2020, **59**, 2562–2574.
35 Y. B. Li, T. Li, X. C. Dai, M. H. Huang, Y. H. He, G. C. Xiao and F.-X. Xiao, *J. Mater.Chem. A*, 2019, **7**, 8938–8951.
36 H. M. Wang, R. Zhao, H. X. Hu, X. W. Fan, D. J. Zhang and D. Wang, *ACS Appl. Mater. Interfaces*, 2020, **12**, 40176–40185.
37 B. Chai, T. Y. Peng, P. Zeng and X. H. Zhang, *Dalton Trans.*, 2012, **41**, 1179–1186.
38 Y. A. Xie, Y. F. Liu, H. L. Cui, W. Zhao, C. Y. Yang and F. Q. Huang, *J. Power Sources*, 2014, **265**, 62–66.
39 S. H. Shen, J. Chen, X. X. Wang, L. Zhao and L. J. Guo, *J. Power Sources*, 2011, **196**, 10112–10119.
40 S. Q. Zhang, X. Liu, C. B. Liu, S. L. Luo, L. L. Wang, T. Cai, Y. X. Zeng, J. L. Yuan, W. Y. Dong, Y. Pei and Y. T. Liu, *ACS Nano*, 2018, **12**, 751–758.
41 Y. Y. Li, J. Y. Cai, M. M. Hao and Z. H. Li, *Green Chem.*, 2019, **21**, 2345–2351.
42 X. C. Dai, M. H. Huang, Y. B. Li, T. Li, B. B. Zhang, Y. H. He, G. C. Xiao and F.-X. Xiao, *J. Mater.Chem. A*, 2019, **7**, 2741–2753.